The Advanced Spectral Library (ASTRAL): Reference Spectra for Evolved M Stars[*]

Kenneth G. Carpenter[1] , Krister E. Nielsen[2], Gladys V. Kober[1,2], Thomas R. Ayres[3] , Glenn M. Wahlgren[4], and Gioia Rau[1,2]

[1] NASA/GSFC Code 667, Goddard Space Flight Center, Greenbelt, MD 20071, USA
[2] Catholic University of America, Washington, DC 20064, USA
[3] University of Colorado, Boulder, CO 80309, USA
[4] General Dynamics Information Technology, 3700 San Martin Drive, Baltimore, MD 21218, USA

Abstract

The *HST* Treasury Program Advanced Spectral Library Project: Cool Stars was designed to collect representative, high-quality UV spectra of eight evolved F−M type cool stars. The Space Telescope Imaging Spectrograph (STIS) echelle spectra of these objects enable investigations of a broad range of topics, including stellar and interstellar astrophysics. This paper provides a guide to the spectra of the two evolved M stars, the M2 Iab supergiant α Ori and the M3.4 giant γ Cru, with comparisons to the prototypical K1.5 giant α Boo. It includes identifications of the significant atomic and molecular emission and absorption features and discusses the character of the photospheric and chromospheric continua and line spectra. The fluorescent processes responsible for a large portion of the emission-line spectrum, the characteristics of the stellar winds, and the available diagnostics for hot and cool plasmas are also summarized. This analysis will facilitate the future study of the spectra, outer atmospheres, and winds, not only of these objects but of numerous other cool, low-gravity stars, for years to come.

Key words: line: formation – line: identification – stars: atmospheres – stars: chromospheres – stars: late-type – stars: winds, outflows

Supporting material: machine-readable tables

1. Introduction

The *Hubble Space Telescope* (*HST*) Treasury Program Advanced Spectral Library (ASTRAL) Project: Cool Stars (PI: T. Ayres) recorded high-resolution, high signal-to-noise spectra of the complete far- to near-ultraviolet wavelength region of stars representing different parts of the evolution of massive cool stars. The spectral library includes spectra for two evolved M stars, α Ori and γ Cru, chosen as representatives for the giant and supergiant luminosity classes. This paper provides an overview of these two reference objects with the intent to provide the tools and basic understanding of evolved stars to assist future mining of the ASTRAL spectral resource.

The outer atmosphere and wind for the giants and supergiants are, in general, not well understood, as they show significant inhomogeneities in their thermal and kinematic structure. In a step toward improved knowledge of these objects, this paper presents identifications of the significant atomic and molecular emission and absorption features observed in α Ori and γ Cru spectra and discusses the character of the photospheric and chromospheric continua. We present the identified fluorescence processes with initial conclusions regarding what information they provide on the physical conditions in the plasma.

The M2 Iab supergiant α Ori (Betelgeuse = HD 39801) is the iconic red supergiant with very clumpy surface convection

(Haubois et al. 2009), distant circumstellar shells (Bernat et al. 1978), and prominent far-ultraviolet (FUV) absorption in carbon monoxide (Carpenter et al. 1994). It is an extreme object in terms of low surface temperature and gravity, high visual luminosity, and lack of coronal signatures and an important transitional object between stars with strong corona and weak winds and objects with weak corona and strong winds. The full UV α Ori spectrum was investigated using *HST*/Goddard High Resolution Spectrograph (GHRS) data ($R \sim 30,000$) in the near-ultraviolet (NUV; Brandt et al. 1995). Its UV spectrum is complex and has weak signatures from the photosphere but is dominated by a warm chromospheric continuum and line spectrum. The emission spectrum shows signatures from fluorescence caused in particular by a strong H I Lyα (Carpenter et al. 1994). Other work on α Ori is presented by Weymann (1962), Boesgaard & Magnan (1975), Boesgaard (1979), and Goldberg (1984) using ground-based observations; Carpenter (1984) with the *International Ultraviolet Explorer* (*IUE*); Carpenter et al. (1994), Carpenter & Robinson (1997), Lobel & Dupree (2000) using *HST*/GHRS data; and Lobel & Dupree (2001) with the *HST*/Space Telescope Imaging Spectrograph (STIS).

The M3.5 III giant star γ Cru (HD 108903) is like α Ori, an extreme noncoronal object with a similar surface temperature but higher surface gravity. Gamma Cru displays a cleaner UV spectrum with more narrow, less blended, but still strong chromospheric and wind emission lines (Carpenter et al. 1995). The object is a bridge star to the warmer, noncoronal K giants, and its clean spectrum is an important guide and tool to understanding both the spectra of the warmer giants and, especially, the more complex spectrum of α Ori, in which the lines suffer significantly more blending with each other and mutilation by overlying absorption. Gamma Cru was observed with *IUE* ($R \sim 20,000$) at most UV wavelengths (Carpenter et al. 1988), though with much lower sensitivity and less depth than is possible with *HST*/STIS. Below 2200 Å, only the

Table 1
STIS ASTRAL Observations for α Ori and γ Cru

Target	Grating	λ_c (Å)	Aperture (arcsec)	Spectral Coverage (Å)	t_{exp} (s)	Mean Julian Date (+2,550,000)
α Ori	E140M	1425	0.20 × 0.20	1150–1700	16132	5599.473
	E230M	1978		1640–2150	11400	5599.525
		2707		2865–3118	1862	5617.910
	E230H	2263	0.20 × 0.09	2132–2393	7554	5615.899
		2513		2386–2649	10404	5600.338
		2762		2622–2875	4704	5600.391
γ Cru	E140M	1425	0.20 × 0.20	1150–1708	17751	5774.729
	E230M	1978		1640–2150	12480	5774.663
		2707		2863–3118	2131	5780.470
	E230H	2263	0.20 × 0.09	2135–2395	8363	5774.550
		2513		2387–2647	8363	5774.596
		2762		2623–2874	5243	5777.726

Note. All of these spectra consist of coadded data sets, and the Mean Julian Date listed represents the starting time of the first segment in the observing sequence. A more comprehensive and detailed description of these observations can be found at http://casa.colorado.edu/~ayres/ASTRAL/.

strongest of the emission features, and no continuum, are visible in the *IUE* spectrum. Higher spectral resolution and signal-to-noise observations with limited spectral coverage were obtained with *IUE* (Carpenter et al. 1988) and GHRS (Carpenter et al. 1995; Rau et al. 2018) and allowed for time-domain studies of the features in these limited wavelength regions. Gamma Cru's UV spectrum is dominated by chromospheric emission, but the photospheric spectrum is visible longward of 2600 Å. The fluorescent spectrum in γ Cru is stronger compared to that in α Ori while no circumstellar shells are observed toward this giant star.

We present the *HST* ASTRAL spectra and some initial results of the analysis. Further papers in this series will include studies of the wind and associated mass loss from these stars.

2. Observations and Stellar Parameters

This paper focuses on the evolved cool stars γ Cru and α Ori and compares their spectral characteristics to the well-studied K1.5 III star α Boo (Hinkle et al. 2005). The observational strategy for α Ori and γ Cru, as for the other objects in the ASTRAL Cool Star Program, was crafted to find the optimal combination of spectral resolution and signal-to-noise over the complete FUV and NUV spectra (1150–3159 Å).

All of the spectra for the two objects are splined in a top-level data set covering the entire wavelength region. These combined spectra are constructed so that the maximum signal-to-noise is achieved in each spectral region, for example, by coadding spectra with high (E140H) and medium (E140M, if available) spectral resolution, after filtering the high-resolution spectrum with the low-resolution point-spread function, and vice versa. This produces a hybrid line-spread function (LSF), which does not influence the analysis of broad-line objects but is significant for narrow-line stellar and/or interstellar features. In such a case, one should examine the highest-resolution coadded spectrum. An overview of the data used in this paper is presented in Table 1, and a more detailed description of the data, including the observing strategy, data reduction, coaddition, and splicing, can be found on the ASTRAL website[5] and at the Mikulski Archive for Space Telescopes (MAST)[6] (doi:10.17909/T9P016).

Lobel & Dupree (2000) derived $T_{eff} = 3500$ K and $\log g = -0.5$ for α Ori based on spectral synthesis calculations at near-infrared wavelengths. These values are in agreement with earlier studies by Carpenter et al. (1994) and Blackwell & Shallis (1977) but are slightly larger than those of Judge & Stencel (1991). The accuracy of the basic stellar parameters for α Ori is hampered by uncertain values for the stellar mass, radius, and distance. Harper et al. (2008) suggested that α Ori is further away than indicated by *Hipparcos* measurements and used the bolometric flux and angular diameter from Perrin et al. (2004) to obtain $T_{eff} = 3650$ K and $\log g = -0.26$. The derived effective temperatures of α Ori in various studies, including Pérez Martínez et al. (2011), converge toward $\sim$3650 K, while the surface gravity is more uncertain.

Gamma Cru was also included in the study by Judge & Stencel (1991) and was assigned $T_{eff} = 3626$ K and $\log g = 0.3$. More recently, Pérez Martínez et al. (2011) derived effective temperatures for a large number of evolved stars, including all three objects in this study, based on basal chromospheric Mg II $k + h$ fluxes measured in *IUE* spectra. The effective temperature for γ Cru from Pérez Martínez et al. (2011) is 3577 K. Ohnaka et al. (2011) presented VLTI/AMBER observations showing a photospheric effective temperature of $T_{eff} = 3690 \pm 54$ K from the limb-darkened disk diameter derived from the *K*-band continuum data.

Alpha Boo (K1.5 III) is one of the brightest stars in the northern sky. Ramírez & Allende Prieto (2011) undertook a comprehensive analysis of α Boo based on model fits of visible–to–mid-IR spectrophotometric data and derived $T_{eff} = 4286$ K. A stellar mass (1.08 $M_\odot$) and radius (25.4 $R_\odot$) for α Boo followed from isochrone fitting and previously reported angular diameter and distance measurements, respectively; these, in turn, implied a surface gravity of $\log g = 1.66$.

The basic stellar parameters of the objects analyzed in this paper are presented in Table 2.

3. Turbulence

The C II intercombination lines at 2325 Å have very low transition probabilities and have been utilized in the past to derive the turbulence in noncoronal K and M stars due to their low opacity ($\tau_0 < 1$; Carpenter et al. 1995; Judge 1986). We have measured the C II lines in the STIS ASTRAL and GHRS pre-COSTAR (i.e., before the aberration correction was

Table 2
ASTRAL M-Star Targets

HD Number	Proper Name	$T_{\rm eff}$ (K)	$\log(g)$	V (mag)	$B - V$ (mag)	Type	Π (″)
39801	α Ori (Betelgeuse)	3650[a]	−0.26[a]	0.42	1.85	M2 Iab	0.006
108903	γ Cru (GaCrux)	3689[b]	0.3[c]	1.63	1.59	M3.5 III	0.037
124897	α Boo (Arcturus)	4286[d]	1.7[d]	−0.04	1.23	K1.5 III	0.089

Notes.
[a] Harper et al. (2008).
[b] McDonald et al. (2017).
[c] Judge & Stencel (1991).
[d] Ramírez & Allende Prieto (2011).

installed on *HST*) γ Cru spectra. The FWHM is corrected for the instrumental profile, STIS 2.2 km s^{-1}, based on fitting the LSF profile at 2400 Å. The instrumental correction for the pre-COSTAR GHRS spectrum is ∼15 km s^{-1} (Carpenter et al. 1994). The line asymmetry, as observed in Carpenter et al. (1995), is weak (see Figure 1) and may be attributed to a fluorescent Fe II line, and no asymmetry is observed in the other C II lines. The measurements are presented in Table 3.

4. Characterization of the Spectra

Alpha Ori and γ Cru both show complex spectra that are dominated by a chromospheric continuum and features from the FUV well into the NUV. Beginning around 2600 Å, the photospheric continuum becomes visible, though chromospheric emission features continue to dominate the spectra to well above 2800 Å. The chromospheric emissions, chromospheric/photospheric absorptions, and wind and molecular absorptions are observed superposed over the chromospheric continuum at short wavelengths and the photospheric continuum at long wavelengths. In α Ori, the spectrum is made more complex by overlying circumstellar absorption.

An overview of the spectra, along with identification of the major features, is shown in Figure 2 and Appendix A. Figure 2 zooms in to show an example of the details in the high-resolution segments between 2320–2380 and 2720–2780 Å, while the appendix shows summary plots of the entire combined spectra. The identifications of the features in the spectra are made using the Kurucz[7] and NIST[8] line databases, in addition to work on the α Boo UV Spectral Atlas (Ayres et al. 1986; Ayres 1986; Hinkle et al. 2005), GHRS studies of λ Vel (Carpenter et al. 1999, 2014), the α Ori study (Carpenter 1984; Carpenter et al. 1994; Carpenter & Robinson 1997; Carpenter et al. 1999), and the γ Cru analysis (Carpenter et al. 1988, 1995). In addition to wavelength coincidence, all expected lines are analyzed based on their intrinsic line strength, e.g., gf value, and a determination of whether all the lines expected from a given energy level (lower if absorption, upper if emission) were observed in the covered wavelength range. For the emission lines characterized as fluorescent, it is required in general that the exciting line and excitation route are identified. Lines and excited levels above those populated in plasma with a temperature of ∼20,000 K or lower were not considered unless a radiative excitation process was found to populate the level. In the following section, the major components observed in the spectra are discussed.

---

[7] http://kurucz.harvard.edu
[8] http://www.nist.gov/pml/data/asd.cfm

Table 3
Turbulence Measurements for γ Cru

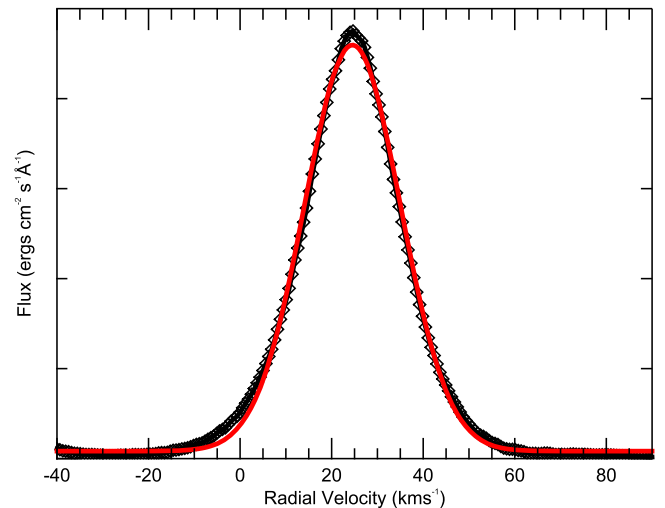| Line (Å, vac.) | RV (km s^{-1}) | | FWHM (km s^{-1}) | |
	STIS	GHRS	STIS	GHRS
C II λ2324.21	24.8	22.2	21.9	22.9
C II λ2325.40	27.7	25.2	23.8	27.6
C II λ2326.11	24.6	24.9	23.3	24.7
C II λ2327.65	25.2	26.5	23.2	25.5
C II λ2328.84	25.7	25.2	24.2	23.6
Mean	25.6	24.8	23.3	24.9

Figure 1. Gaussian fit of C II λ2325.40 in the γ Cru spectrum. The asymmetry (enhancement) of the blue wing that was observed in the 1995 GHRS data (Carpenter et al. 1995) and is strong in the α Ori spectrum is weak in this 2011 STIS spectrum of γ Cru (diamonds: observed spectrum; red line: fitted spectrum).

4.1. The Chromospheric Continua

These objects display a strong FUV continuum whose flux is orders of magnitude brighter than expected from the photospheres of M giant or supergiant stars. The excess flux is thought to be formed in the chromosphere. Although it is visible in earlier *IUE* data, the chromospheric continuum emission was only understood to be present after GHRS observations of α Ori were obtained and analyzed to reveal that the FUV spectrum was dominated by substantial circumstellar CO *A–X*–band absorptions superposed over a chromospheric continuum, rather than just a collection of blended chromospheric emission lines (Carpenter et al. 1994). The
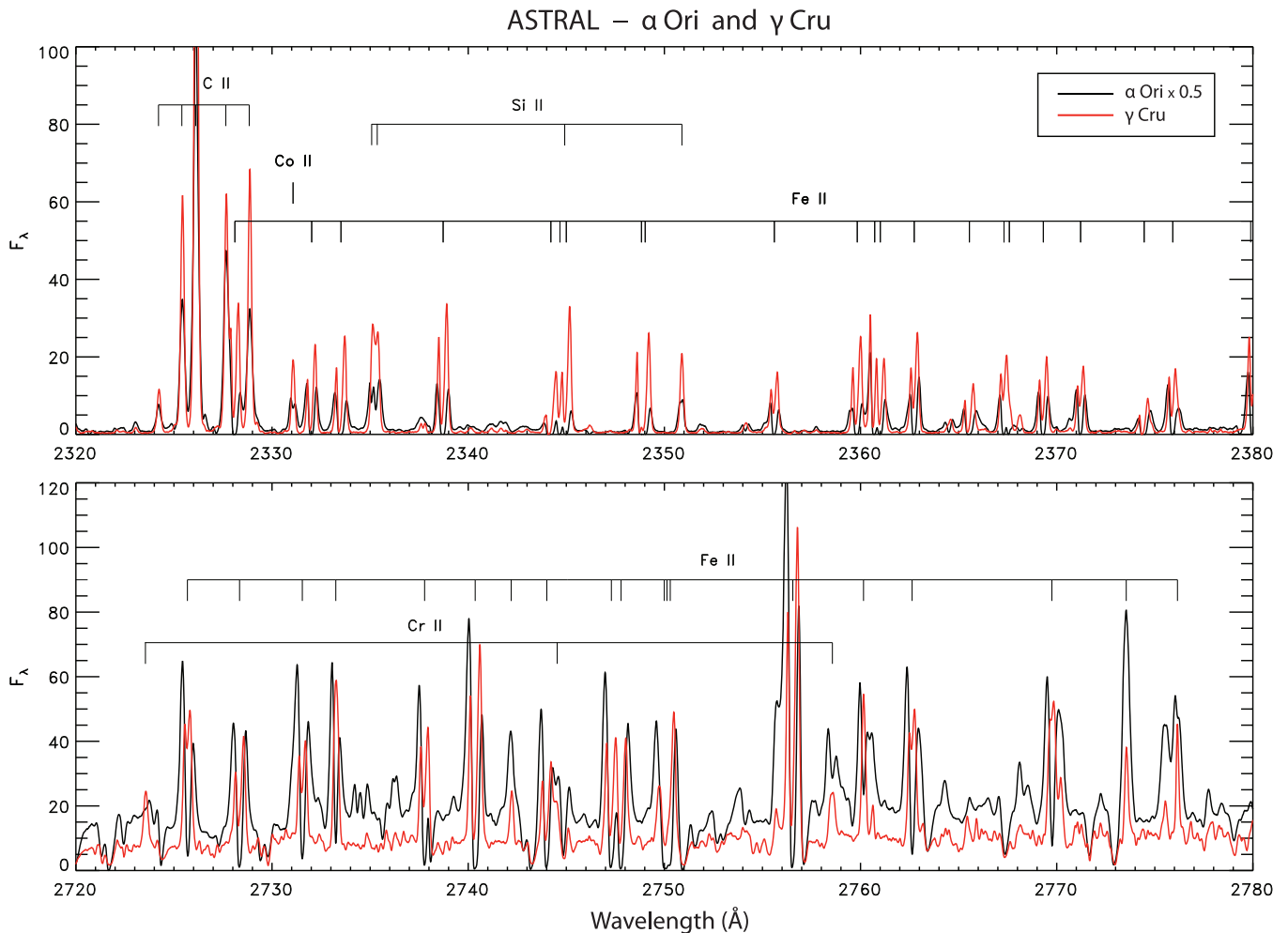
Figure 2. The wealth of detail in these spectra is illustrated in these two zoomed-in panels, showing the 2320–2380 and 2720–2780 Å spectral regions. Selected emission lines are identified. The flux is in units of 10^{-13} erg cm^{-2} s^{-1} Å^{-1}.

FUV continuum has also been observed in the K5 supergiant λ Vel (Carpenter et al. 2014), but it is more uniform for λ Vel due to the absence of the CO ($A-X$) absorption bands. The continua for α Ori and γ Cru are presented in Figures 3 and 4, respectively, where the observed flux in the optical (Kiehling 1987) and UV (ASTRAL) wavelength regions are compared to a computed flux using an ATLAS9 model.[9] The calculations of the observed surface fluxes for α Ori and γ Cru are based on angular diameters of 43.8 mas (Perrin et al. 2004) and 24.7 mas (Glindemann et al. 2001) for α Ori and γ Cru, respectively.

The observed and modeled fluxes are in agreement for both objects down to ~3500 Å, but in the UV, the fluxes diverge and differ by 5–6 orders of magnitude below 2000 Å. Carpenter et al. (1999, 2014) compared the flux for λ Vel with a model where the temperature in the upper layers was not allowed to fall below a minimum temperature of 3200 K ($T_{\min}/T_{\rm eff} = 0.8$) that reproduced the flux level for λ Vel down to 2000 Å significantly better but could not reproduce the flux at shorter wavelengths. The observed flux requires the presence of a temperature rise (as shown in Figures 3 and 4) above the photospheric value and even above the 3200 K temperature minimum; thus, the origin of the flux is in the chromosphere.

The γ Cru and α Ori continua show similar behavior with an even larger flux discrepancy at UV wavelengths.

4.2. The Emission Spectrum

The emission spectrum in α Ori and γ Cru is strongly influenced by the radiation of strong chromospheric features and the surface blackbody radiation. Many of the light elements with low ionization limits are ionized and show recombination spectra, while other ions and molecules show strong signatures of selective excitation processes. We provide details of our identifications and measurements of the emission lines in the ASTRAL spectra of α Ori and γ Cru in Appendix B, where Tables 7 through 9 show, respectively, the measured properties of (1) the fluorescent emission lines in α Ori and γ Cru, (2) the chromospheric and wind lines in γ Cru, and (3) the chromospheric and wind lines in α Ori. The following paragraphs briefly discuss the presence of some of the observed spectral features in the α Ori and γ Cru spectra.

4.2.1. Atomic Emission

The ionization potential for neutral sulfur is close to the H I Lyα transition energy; hence, the hydrogen radiation populates numerous levels close to the S^0 ionization limit (Tondello 1972; Judge 1988). The cascades to the ground state
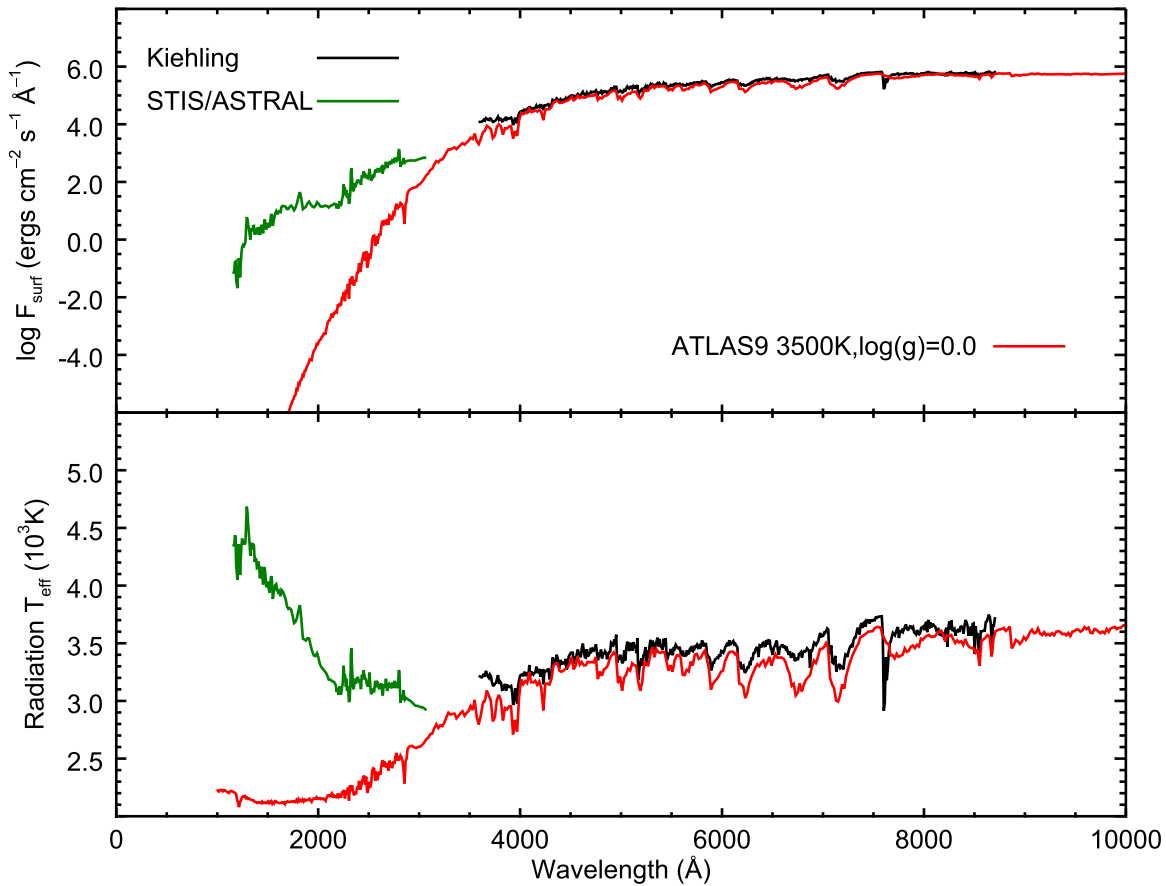

Figure 3. Top: comparison of the observed continuum surface flux distribution from α Ori with a modeled Kurucz LTE ATLAS9 synthetic continuum. Observed optical data (black) are from Kiehling ([1987](#)), UV data are from *HST*/STIS (green), and synthetic continua were computed with a standard Kurucz model (red). Orders of magnitude separate the observed UV from the photospheric models; there is clear evidence of continuum emission from the hotter chromospheric layers. Bottom: chromospheric temperature rise implied by the observed fluxes (black and green lines) shown in a plot of the effective radiation temperature vs. wavelength. The Kurucz model temperature vs. wavelength is also shown for comparison.

produce a prominent S I emission spectrum in both α Ori and γ Cru (see panel 3 of Figures [5](#) and [10](#) and panels 2, 3, and 5 of Figure [11](#)). Similarly, the H I Lyα flux is important for C^0 and Si^0 so that both can be ionized by the strong hydrogen flux and for the formation of the C I, C II, Si I, and Si II spectra. Neutral carbon can be ionized from the ^{1}D (10, 192 cm^{-1}) and ^{1}S (21, 648 cm^{-1}) terms and form a prominent C I spectrum, particularly at wavelengths below 2000 Å (some examples can be seen in panels 3 and 5 of Figure [10](#) and panel 3 of Figure [11](#)). The neutral carbon spectrum is stronger in γ Cru than α Ori, indicating either a weaker H I Lyα or a lower carbon abundance in α Ori, but both spectra show a similar disproportional strength to C I λ1657 and C I λ1993 (see panel 5 of Figure [10](#) and panel 3 of Figure [11](#)) that is caused by differences in the optical depth sensitivity (Jordan [1967](#)). Neutral silicon shows a greater presence in α Ori, with stronger emission lines from the excited levels ($E_{low} > 6000$ cm^{-1}) but exclusively absorption or self-reversed line profiles for the resonance lines.

Selective fluorescence processes in cool giants and supergiants have previously been observed for the iron-group elements and discussed by Carpenter et al. ([1994](#), [1995](#)). These excitation channels are enabled by strong chromospheric emission, lines such as H I Lyα and H I Lyβ, that produce observed fluorescence in, for example, O I, Cr II, and Fe II. The strong neutral oxygen spectrum observed in both α Ori and

γ Cru is caused by the wavelength coincidence of O I λ1026 and H I Lyβ populating the $3d^3$D state at 97,488 cm^{-1}. Cascades from this upper level produce the prominent O I 1355 Å (UV1), O I triplet at 1300 Å (UV2), and O I λ1641 in both objects (see panels 2 and 5 of Figure [10](#)).

The H I Lyα-driven Fe II fluorescence is strong in both α Ori and γ Cru. The rich Fe II spectrum has multiple transitions close in wavelength (<3 Å) to the strong H I Lyα line, resulting in numerous fluorescent transitions from Fe$^+$ levels between 90,000 and 110,000 cm^{-1} (see Table [4](#)). The strong H I Lyα also redistributes the population in the Fe$^+$ ground configurations, enabling additional fluorescence processes from higher metastable levels ($E_{low} > 20,000$ cm^{-1}) that normally would not be populated in this environment. For example, Johansson & Jordan ([1984](#)) showed that the levels at 107,674 and 107,720 cm^{-1} can be excited by H I Lyα. Some decays from the pumped levels fall outside our covered wavelengths but produce observable secondary fluorescence noticeable in γ Cru, for example, Fe II $\lambda\lambda$2521, 2527, and 2539.

The Cr$^+$ lines reflect an H I Lyα fluorescence spectrum that is weaker than that for Fe II. The majority of the strong pumping channels in Fe$^+$ originate from Fe$^+$ metastable states 7955–8846 cm^{-1}, while the lowest energy levels in Cr$^+$ with H I Lyα coincidence are slightly higher, at $\sim$12,000 cm^{-1}. The levels at 94,749 and 94,656 cm^{-1} show a strong influence from H I Lyα and, to a lesser degree, the energy levels at 94,522,
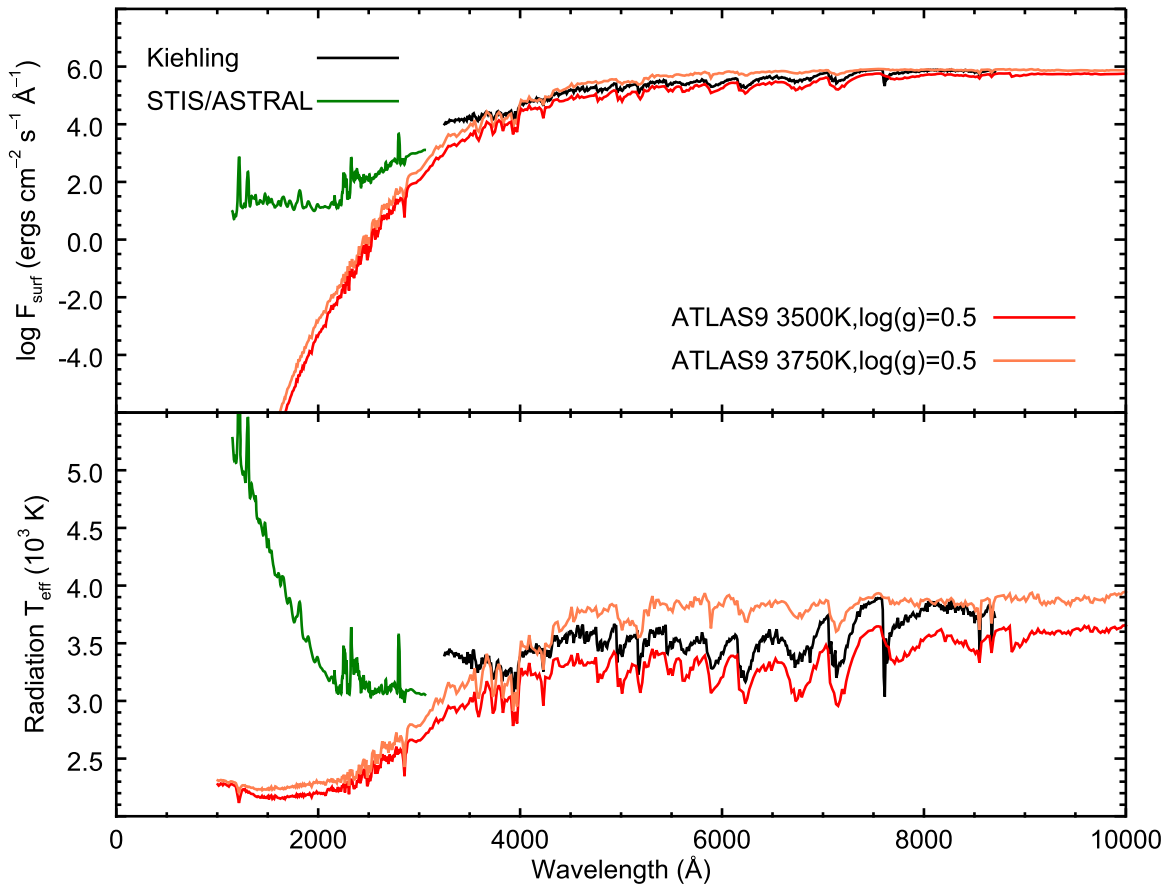
Figure 4. Top: continuum for γ Cru, shown as in Figure 3 for α Ori. The modeled Kurucz LTE ATLAS9 flux (3500 K in red; 3750 K in orange) is compared to the observed flux by Kiehling (1987) in the optical and ASTRAL flux in the UV. Bottom: chromospheric temperature rise implied by the FUV continuum in γ Cru. The Kurucz model temperature vs. wavelength is also shown for comparison.

94,365, 94,452, 94,363, and 102,725 cm^{-1}. No secondary fluorescence, analogous to that observed from Fe$^+$, is observed from Cr$^+$ in the γ Cru or α Ori spectra.

The existence and productivity of a fluorescent pumping mechanism is dependent not only on the wavelength coincidence but also on the strength and width of the exciting feature. Other chromospheric features that are sufficiently strong and broad and have important coincidences with strong lines of other elements are C$^+$, O^0, Mg^0, Mg$^+$, Si$^+$, and even Fe$^+$—all of which provide weaker but similar excitation routes as H I Lyα and H I Lyβ.

Some of the other iron-group ions show signs of fluorescence, including Fe I, Mn I, Ti II, Ni II, and Co II. Neutral iron displays a strong wind absorption spectrum from the ground configuration, especially in α Ori. The strongest ground-state transitions are also present in the γ Cru spectrum, and Fe^0 seems to have a strong population even in the first excited configuration. Accidental wavelength coincidences between Fe I transitions from the a^5F term and the strong Mg II $\lambda2796.35$, Fe II $\lambda2725.69$ result in a fluorescent transition above 2600 Å. A single line as a result of Fe I coincident with Mg I λ 2853 is present in the α Ori spectrum at 2838 Å.

The O I $\lambda\lambda1304$, 1305, 1306 (that are cascades from H I Lyβ pumping) give, while weaker in α Ori, a strong fluorescent CO spectrum (as discussed in Section 4.2.2) in γ Cru in addition to P II $\lambda1309.87$. The latter is influenced by the resonance wind lines in α Ori. The C II $\lambda1335.73$ produces the Cl I $\lambda1351.6$

line, a process originally reported by Shine (1983), and likely Fe II $\lambda\lambda2492$, 2303 in γ Cru. All of the C II pumped features are absent or very weak in the α Ori spectrum, which is consistent with the intrinsic strength of the singly ionized carbon spectrum. Magnesium and silicon transitions selectively excite a few levels for the iron-group elements.

Transitions from levels <90,000 cm^{-1}, which are below what can be excited by H I Lyα, are observed in both α Ori and γ Cru in Ti$^+$, Cr$^+$, Fe$^+$, Ni$^+$, and Co$^+$. These levels are selectively populated by strong Fe II transitions. Some of these processes involving strong Fe II transitions are described by Carpenter & Johansson (1988), but the impact of the strong Fe II chromospheric wind spectrum and the energy-level density for the iron-group elements enable a large number of wavelength coincidences that produce numerous excitation channels. The levels sp x^{6}P (79,246, 79,285, and 79,331 cm^{-1}) are examples of levels pumped by Fe II UV9 between 1260 and 1275 Å to produce fluorescent lines at 1780 Å, Fe II UV 191. The Fe II UV9 to UV 191 photon conversion was first described by Hempe & Reimers (1982). Johansson et al. (1995) later discussed the presence of satellite lines close to the 1785, 1786, and 1788 lines, due to level mixing between w^{2}P and x^{6}P. No satellite lines are resolved in the spectra of γ Cru or α Ori. Hempe & Reimers (1982) reported that almost every photon to the x^{6}P levels is redirected to UV 191 instead of being reemitted in UV9.
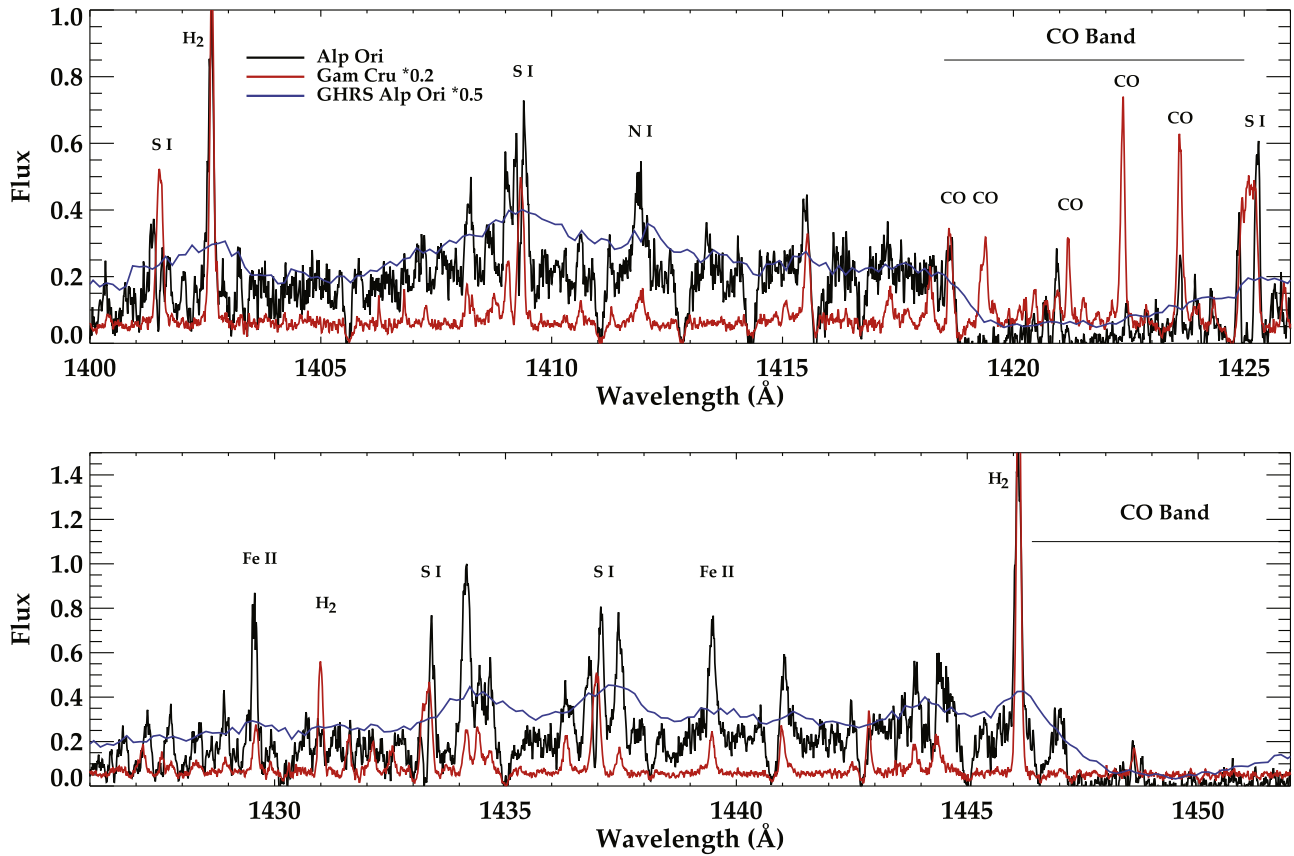
Figure 5. The search for cool plasma in these two stars: the 1400–1452 Å region of the ASTRAL α Ori and γ Cru spectra, with a lower-resolution GHRS spectrum of α Ori superposed to show its circumstellar CO $A-X$ absorption bands. Note the narrow fluorescent CO emission lines that are superposed over the much broader CO absorption bands. The CO absorption bands are signatures of cool material in the circumstellar shells of α Ori, while the fluorescent CO emission in both stars is a signature of cool material embedded in their chromospheres. Fluxes are in units of 10^{-13} erg cm^{-2} s^{-1} Å^{-1}.

Table 4
Fe$^+$ Energy Levels Populated via H I Lyα λ1215 Wavelength Coincidence

E_u (cm^{-1})	E_l (cm^{-1})	λ (Å)	$|\delta\lambda|$	log gf
90,067[a]	7,955	1217.848	2.17	−1.49
90,398	7,955	1212.966	2.71	−1.47
90,639	7,955	1215.852	0.18	−2.03
90,899	8,680	1216.272	0.60	−2.35
91,200	8,846	1214.285	1.39	−2.16
90,301	7,955	1214.398	1.28	−2.23
90,387	7,955	1213.132	2.54	−1.18
90,630	8,391	1215.983	0.31	−3.05
90,781	7,955	1213.759	1.91	−1.17
91,071	8,680	1213.738	1.94	−1.31
91,209	8,846	1214.150	1.52	−1.49
90,839	8,680	1217.152	1.48	−2.22
90,901	8,680	1216.239	0.57	−2.32
91,048	8,846	1216.523	0.85	−2.30
95,858	13,673	1216.769	1.10	−3.79
95,996	13,673	1214.735	0.94	−3.07
103,967	21,812	1217.205	1.53	−2.08
104,817	22,637	1216.847	1.17	−1.47
104,938	22,637	1215.058	0.62	−1.78
105,029	22,810	1216.275	0.60	−1.97
107,674	25,428	1215.873	0.20	−1.34
107,721	25,428	1215.183	0.49	−1.50

Note.
[a] 5p $^4F_{9/2}$ at 90,043 cm^{-1} is pumped via energy-level mixing with 5p $^4G_{9/2}$ 90,067 cm^{-1}.

Table 5
H$_2$ Transitions with H I Lyα λ1215 Wavelength Coincidence and Populated Energy Levels

λ (Å)	ID	E_l (cm^{-1})	E_u (cm^{-1})
1214.465	H$_2$(3-1)R15	15,649	97,990
1214.781	H$_2$(4-3)P5	13,265	95,584
1215.727	H$_2$(1-2)R6	10,261	92,516
1216.070	H$_2$(1-2)P5	9,654	91,886
1217.205	H$_2$(0-2)R0	8,086	90,242
1217.643	H$_2$(0-2)R1	8,193	90,319
1217.904	H$_2$(2-1)P13	13,191	95,299

4.2.2. Molecular Emission

Molecular emission is observed in the form of fluoresced CO and H$_2$ emission, as seen in the K-giant stars α Boo (K1.5 III) and α Tau (K5 III). Molecular hydrogen is the most abundant species in the interstellar medium and is fundamental for the formation of complex molecules and dust. In most systems, the temperature limits the population to the lowest J-states in the ground vibrational level. This results in observable transitions only in the FUV, in addition to rotational lines in the infrared. The H$_2$ energy levels populated by coincidence with H I Lyα are shown in Table 5. Carbon monoxide is like H$_2$, an abundant interstellar molecule with relatively simple spectroscopic properties. The energy-state population in carbon monoxide is restricted to its

lowest vibrational states in cool-temperature environments, and the chromospheric conditions enable population of higher states and hence pumped transitions in our observed wavelength interval. The most prominent spectrum in the UV is the fourth positive system, $A\,^1\Pi - X\,^1\Sigma^+$, with transitions between 1280 and 2800 Å; however, our identifications are exclusively between 1330 and 1554 Å. Fluorescent carbon monoxide has previously been observed in α Boo (Ayres et al. 1981, 1999) and α Tau (McMurry & Jordan 2000).

The molecular fluorescence is stronger in γ Cru than for α Ori. The H_2 and CO spectra are powered by H I Lyα and O I $\lambda\lambda$1302, 1304, 1306, respectively. The large number of energy levels and their closeness in energy result in several lines in both H_2 and CO with wavelengths close to the pumping transitions. Other pumped channels for CO may include H I Lyα and C I λ1656–1658, but fluorescence fed by these transitions is not identified in either γ Cru or α Ori. These CO and H_2 fluorescence spectra are believed to be formed in the objects' outer atmosphere, and by studying them, information regarding the physical structure of the emitting gas and the radiative source from the inner parts is gained. Alpha Boo and α Tau do not show the strong FUV continuum observed for α Ori and γ Cru, which is consistent with the greater column densities of the cooler and more massive M-star chromospheres, where $\tau = 1$ surfaces are shifted to larger radii as the chromospheric continuum is formed further out at a greater temperature and producing a larger surface flux.

The CO fluorescence in α Ori is more difficult to analyze, due to the circumstellar shell engulfing the object. The circumstellar absorption is strong and makes the identification of some of the fluorescent CO lines uncertain.

We have measured the fluorescent atomic and molecular emission-line features and present the line identifications, wavelengths, integrated and surface fluxes, and apparent velocity relative to the stellar photospheric radial velocity (RV) in Table 7 in Appendix B.

4.3. Diagnostics of Cool Plasma

The spectra of both stars contain numerous diagnostics of cool plasma, including the atomic emission as shown in Figure 5 from chromospheric S I and N I, as well as fluorescent molecular H_2 and CO emission from low-temperature pockets of material immersed in the chromosphere. In addition, the spectrum of α Ori contains broad CO $A-X$ bands produced in its circumstellar shells (Bernat et al. 1978; Carpenter et al. 1994).

Strong absorption bands of the CO $(A-X)$ system are observed in the α Ori FUV spectrum, but there is no evidence of their presence in the λ Vel or γ Cru spectra. However, there are clear bands of the OH molecule in both of the M stars, which show a major band head of OH at 2811 Å.

4.4. Diagnostics of Hot Plasma

A search was conducted for spectral features from C II, C IV, Si III, Si IV, and N V as indicators of hot plasma in the envelopes of γ Cru and α Ori, as shown in Figure 6. The α Ori and γ Cru spectra are compared to a reference spectrum of the coronal-type F5 IV star α CMi. All of the hot plasma diagnostics are present in the α CMi spectrum. The C II λ1335 is the hottest diagnostic ($\sim 2 \times 10^4$ K) seen in these two M stars, γ Cru and α Ori.
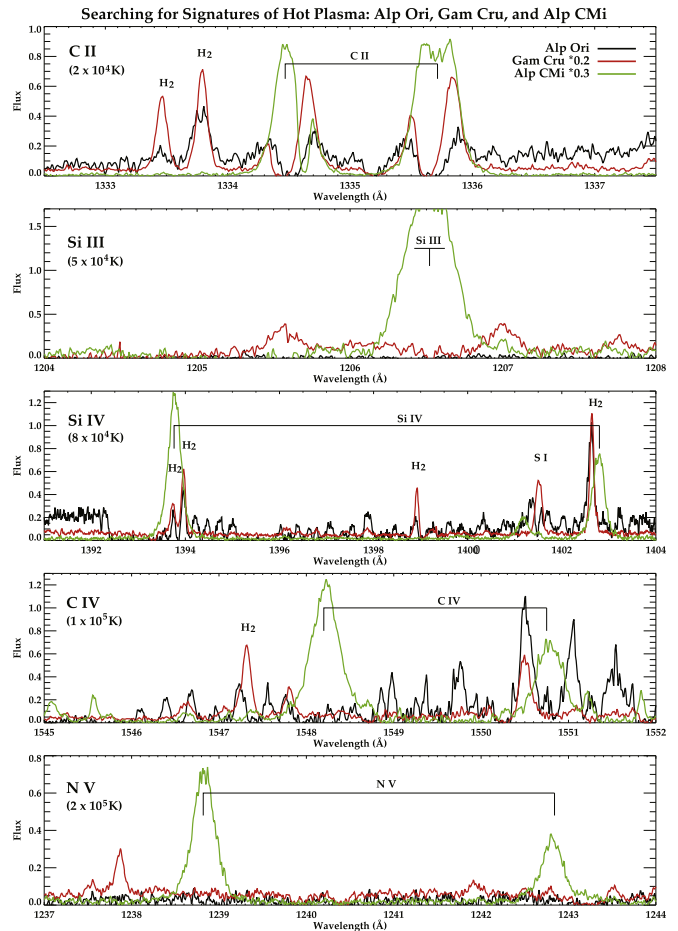

Figure 6. Search for evidence of hot plasma in α Ori and γ Cru for the regions around five lines indicative of temperatures ranging from 2×10^4 to 2×10^5 K. The approximate formation temperature of each line is given in parentheses for the section of spectral diagnostics. Flux is in units of 10^{-13} erg cm^{-2} s^{-1} Å^{-1}.

5. Comparison with Spectrum of α Boo

In Figures 7–9, we compare profiles for a set of atomic (Fe II) emission lines and two sets of molecular (H_2 and CO) emission lines in the two M stars α Ori and γ Cru to those in the prototypical K1.5 giant α Boo. In Table 6, we show the surface fluxes for the chromospheric emission components of these lines as a proxy of the magnetic activity levels (Fe II) and the efficiency of the fluorescence mechanisms (H_2 and CO) in the outer atmosphere of each star.

The lines of Fe II in Figure 7 are chosen to represent a wide range in profiles, but it is clear that the strength of the overlying wind absorption is always much stronger in a given line in α Ori than in the other two stars, while the lines in α Boo are both narrower and weaker in their chromospheric emission and have very mild, if any, wind absorption superposed. If we examine the Fe II surface fluxes in Table 6 of these lines in the three stars, we see that the fluxes are generally substantially larger in the two giant stars γ Cru and α Boo versus the uniformly weaker lines in the supergiant α Ori.

The lines of H_2 in Figure 8 are generally similar in the two giant stars α Boo (K1.5) and γ Cru (M3.4), though the latter has systematically stronger surface fluxes. The lines in the M supergiant α Ori (M2 Iab), in contrast, are considerably weaker
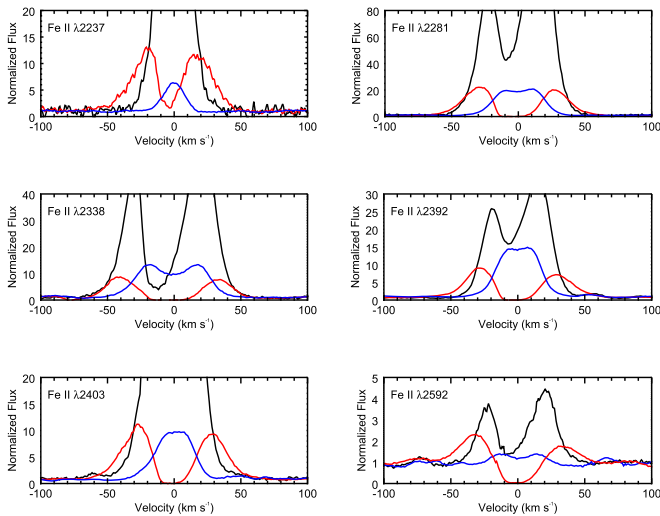
Figure 7. Spectral comparison of the Fe II line profiles observed in γ Cru (black), α Ori (red), and α Boo (blue). Plots are normalized to continuum 50–100 km s^{-1} from line center.

Figure 8. Spectral comparison of the H$_2$ line profiles observed in γ Cru (black), α Ori (red), and α Boo (blue).

Table 6
Comparison of Selected Surface Fluxes from α Ori, γ Cru, and α Boo
Integrated Line Surface Fluxes in Units of erg cm^{-2} s^{-1}

Lines	Wavelength (Å, vac.)	α Ori F_{surf}	γ Cru F_{surf}	α Boo F_{surf}
Fe II	2237.4	83.7	98.8	105.7
	2280.6	800.4	2566.8	2362.2
	2338.7	927.7	3160.6	3306.0
	2392.2	1305.0	3043.1	1955.6
	2403.3	798.4	1235.9	2686.3
	2592.3	391.3	704.2	356.0
H$_2$	1402.65	1.7	22.4	20.2
	1446.12	3.3	50.6	21.0
	1333.80	0.9	15.3	13.6
	1504.76	3.1	45.9	19.5
	1524.66	2.8	25.4	7.6
	1562.39	0.3	12.8	8.6
CO	1343.49	0.5	13.4	14.9
	1423.61	0.3	14.3	14.6
	1382.64	0.7	27.5	30.7
	1378.69	⋯	24.5	37.1

Figure 9. Spectral comparison of the CO line profiles observed in γ Cru (black), α Ori (red), and α Boo (blue).

in both observed flux (at Earth) and surface flux than the lines in either of the two giants.

The CO lines in Figure 9 are also uniformly much stronger in the two giant stars than in the M supergiant, in which the CO emission is very weak, which may be due in part to substantial CO absorption in the circumstellar shell around α Ori. The surface fluxes in the two giants are very similar, while in α Ori, the fluxes are very small in three of the lines and unmeasurable in the fourth line.

6. Summary

We have presented a detailed overview of the definitive STIS UV high-resolution spectra of two evolved M stars, M2 Iab supergiant α Ori and the M3.4 giant γ Cru, obtained as part of the *HST* Treasury Program Advanced Spectral Library (ASTRAL) Project: Cool Stars to facilitate the use of this impo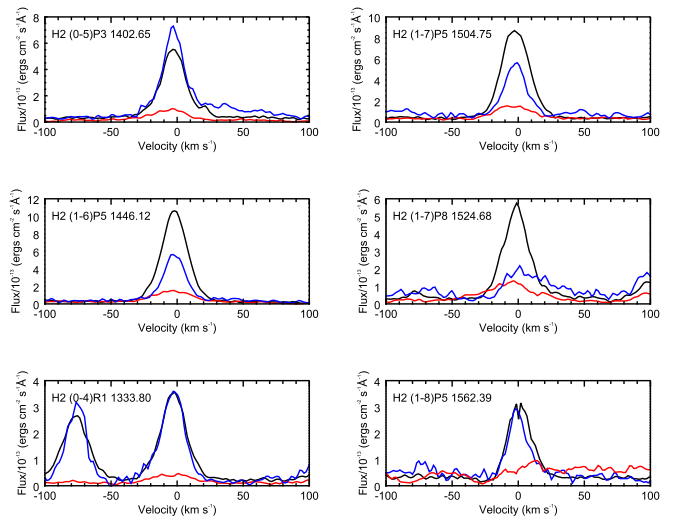rtant archival data set by future investigators. This study provides identifications of the significant atomic and molecular emission and absorption features and discusses the characteristics of the line spectra. The strong chromospheric continua seen in the FUV and mid-UV are quantified, and the merger of these continua with the photospheric continua seen at longer wavelengths is discussed. The fluorescent processes responsible for a large portion of the emission-line spectrum, the characteristics of the stellar winds, and the available diagnostics for hot and cool plasmas are summarized. Finally, we have discussed the differences between these spectra and the existing UV spectra of the prototypical K1.5 III giant α Boo to illustrate the changing nature of the spectra as one moves from the K giants into the cooler M stars.

Other recent work on α Ori may be useful in understanding and putting these UV observations in context. Perhaps most significant is the Petit et al. (2013) report of a detection of a surface magnetic field in α Ori using a time series of six circularly polarized spectra obtained using the NARVAL spectropolarimeter at Telescope Bernard Lyot (Pic du Midi Observatory (F)) between 2010 March and April. Zeeman

signatures were repeatedly detected in cross-correlation profiles, corresponding to a longitudinal component of about 1 G and showing a smooth increase of the longitudinal field from 0.5 to 1.5 G that correlated with RV fluctuations. The correlation of Stokes V with RV fluctuations and their redshift of about 9 km s^{-1} with respect to the Stokes I profiles suggest that the observed magnetic elements may be concentrated in the sinking components of the convective flows. Tessore et al. (2017) followed this up by investigating whether the magnetic field found on α Ori was typical of red supergiants (RSG) and found that the two red supergiant stars in their sample, CE Tau and μ Cep, display magnetic fields very similar to that of α Ori. They further reported that their nondetection of a magnetic field on the post-RSG star ρ Cas suggests that the magnetic field disappears, or at least becomes undetectable with present methods, at later evolutionary stages, and that their analysis of α^1 Her supports the proposed reclassification of the star as an M-type asymptotic giant branch star. Wood et al. (2016) discussed constraints on the winds and astrospheres of red giant stars provided by *HST* observations, focusing on the spectra of the Mg II H and K lines near 2800 Å. They studied stellar chromospheric emission, winds, and astrospheric absorption, concentrating on spectral types between K1.5 III and M5 III (noncoronal stars that possess strong chromospheric winds).

They found a very tight relation between Mg II surface flux and photospheric temperature, supporting the notion that all K2–M5 III stars are emitting at a basal flux level. Wind velocities are generally found to decrease with spectral type, from $\sim$40 km s^{-1} at K1.5 III to $\sim$20 km s^{-1} at M5 III. The power-law index in the Wood et al. (2016) empirical relation $F_{\mathrm{Mg\,II}} \sim T_{\mathrm{eff}}^{9.1}$ is remarkably close to the index of a theoretical relation derived by Bohn (1984) linking the flux of acoustic power F_{acoustic} and the effective temperature: $F_{\mathrm{acoustic}} \sim T_{\mathrm{eff}}^{9.75}$. This makes it highly likely that the basal flux is indeed related to acoustic power, rather than magnetic effects (we thank the anonymous referee for pointing this out to us).

Appendix A
Full-spectrum Plots

Figures 10–13 show the full ASTRAL spectra of the M stars γ Cru and α Ori.

Figure 10. The 1200–1700 Å spectral region. Selected emission lines are identified. Flux is in units of $10^{-13} \, \mathrm{erg} \, \mathrm{cm}^{-2} \, \mathrm{s}^{-1} \, \mathrm{\AA}^{-1}$.

ASTRAL − α Ori and γ Cru

Figure 11. The 1700–2200 Å spectral region. Selected emission lines are identified. Flux is in units of $10^{-13}\,erg\,cm^{-2}\,s^{-1}\,Å^{-1}$.

Figure 12. The 2200–2700 Å spectral region. Selected emission lines are identified. Flux is in units of 10^{-13} erg cm^{-2} s^{-1} Å^{-1}.

ASTRAL − α Ori and γ Cru
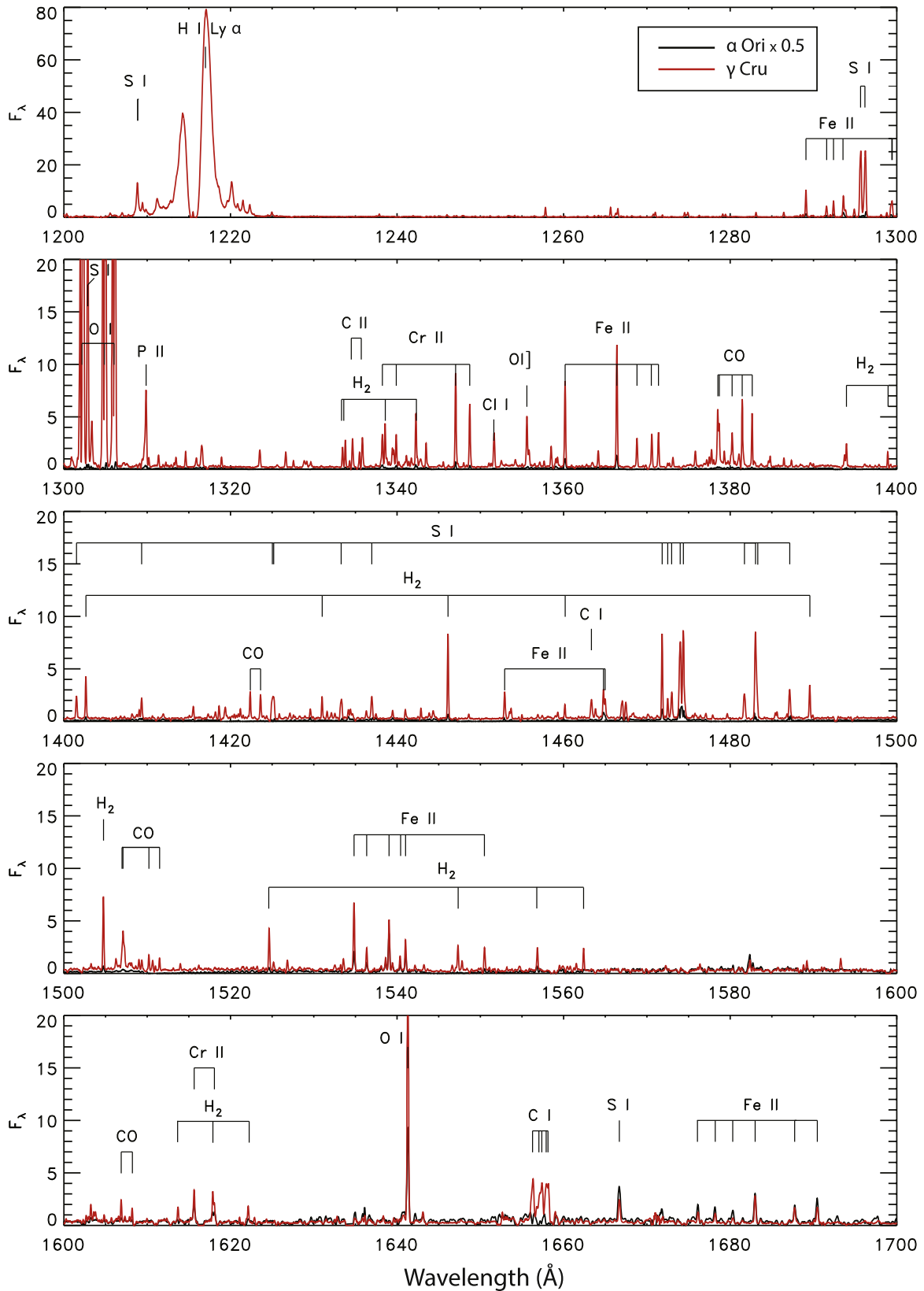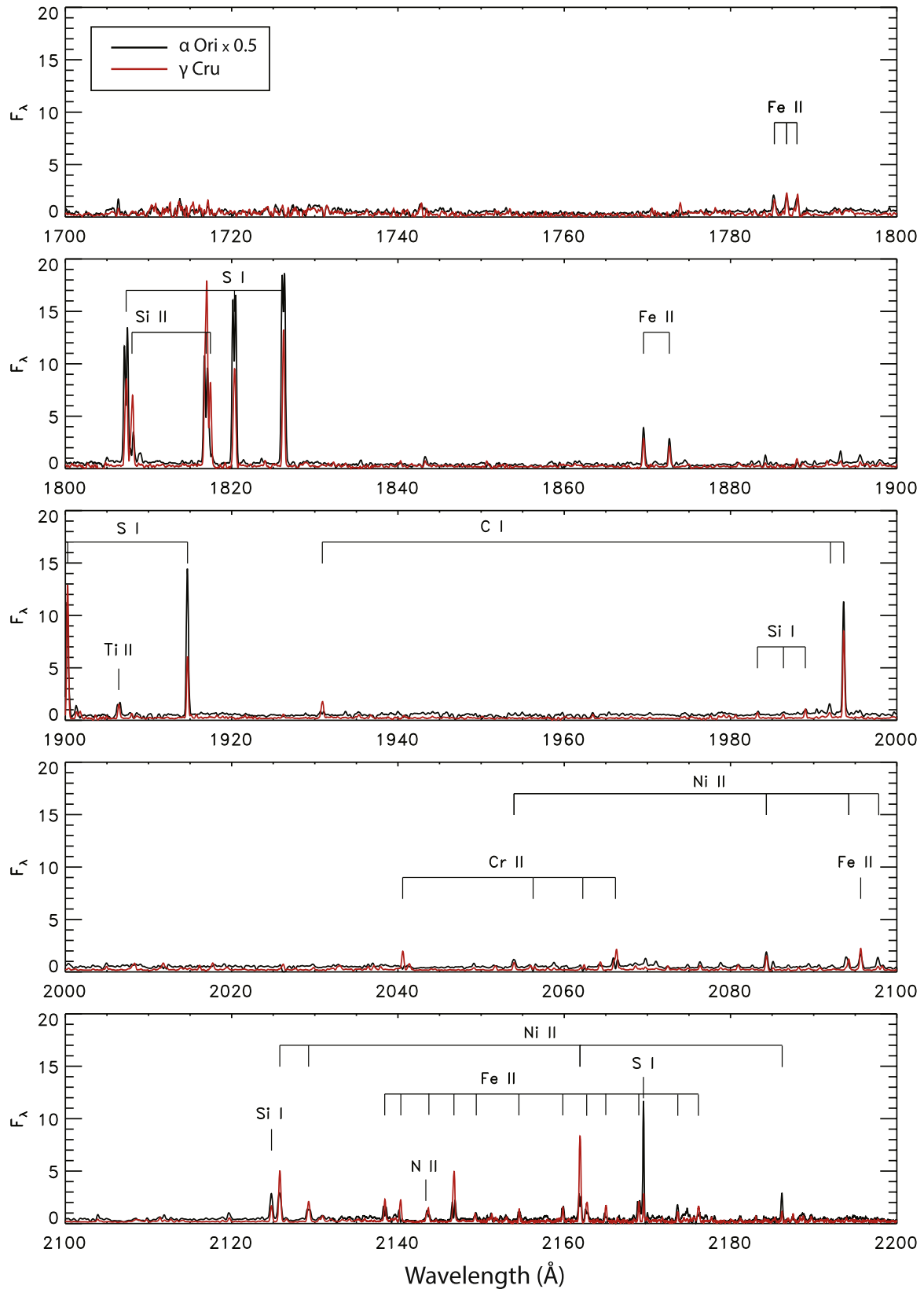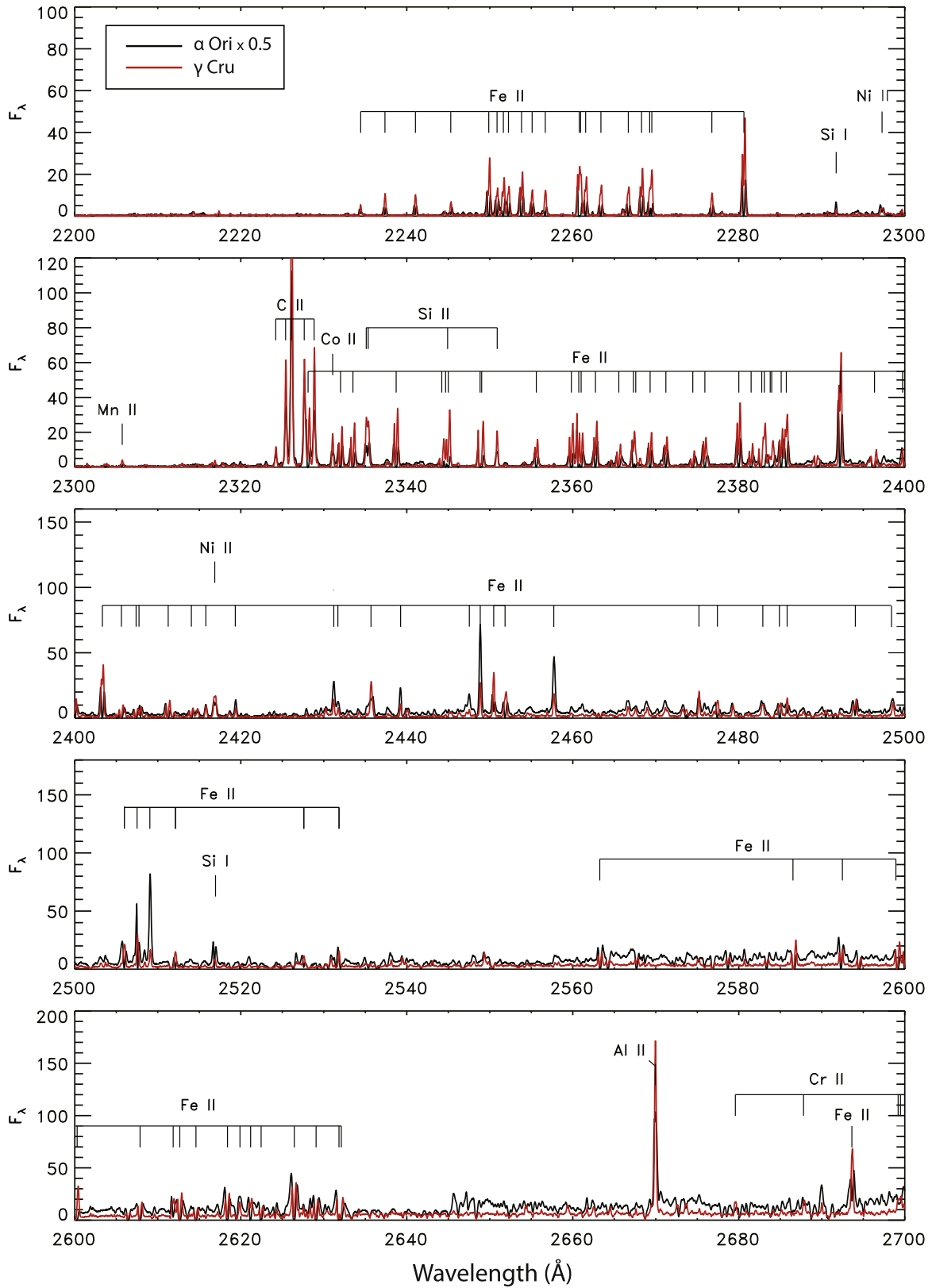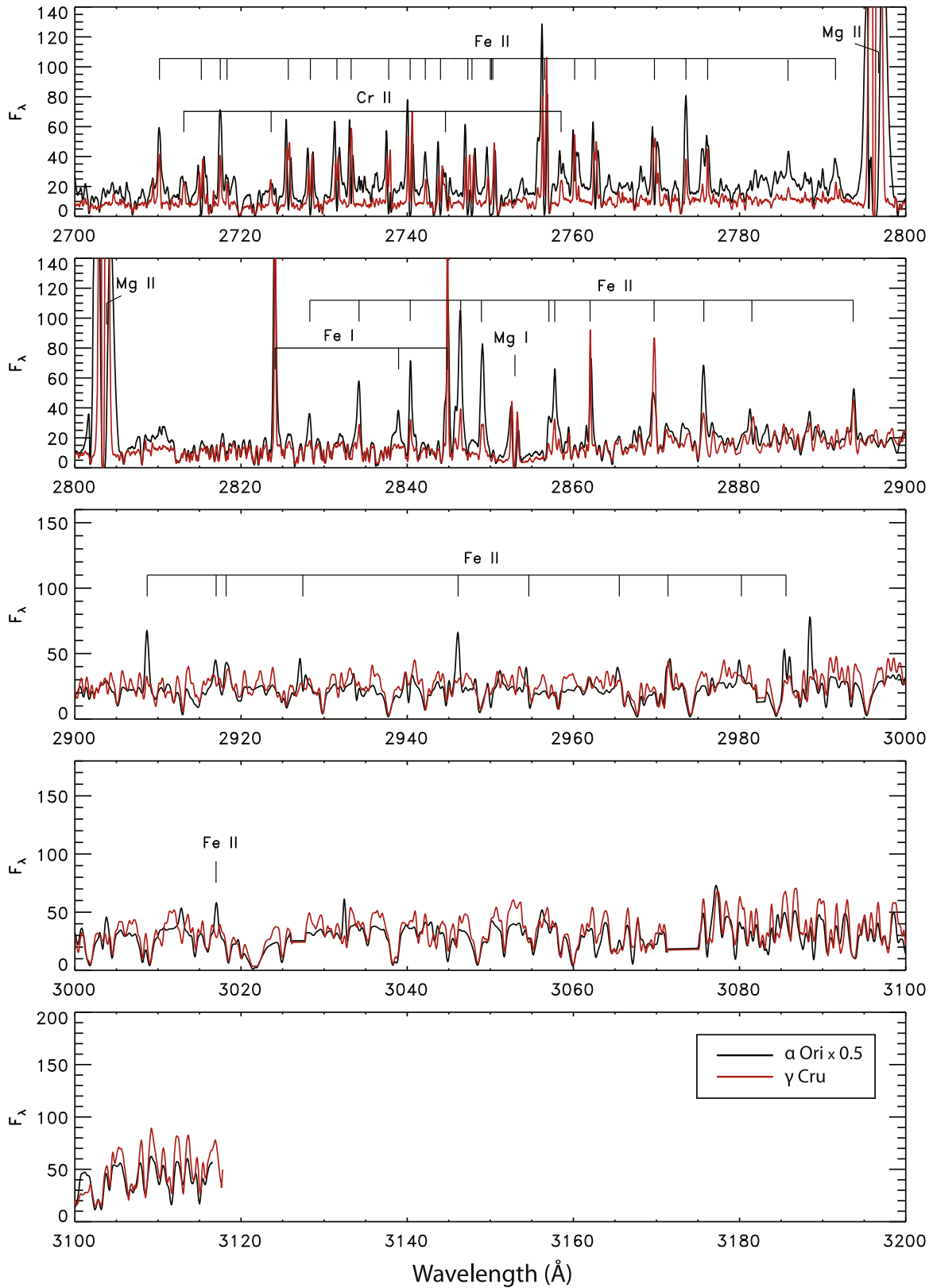

Figure 13. The 2700–3120 Å spectral region. Selected emission lines are identified. Flux is in units of 10^{-13} erg cm^{-2} s^{-1} Å^{-1}.

Appendix B
Detailed Tables: Emission-line Measurements

Tables 7–9 show, respectively, the measured properties of (1) the fluorescent emission lines in α Ori and γ Cru, (2) the chromospheric and wind lines in γ Cru, and (3) the chromospheric and wind lines in α Ori. The RVs shown in these tables are relative to the photosphere (stellar RVs of 20.6 km s^{-1} for γ Cru and 21.9 for α Ori have been subtracted from the measured values). We show in the tables the most up-to-date laboratory atomic and molecular-line data in the literature, taken primarily from the Kurucz (see footnote 7) and NIST[10] line databases.

Table 7
Properties of Fluorescent Emission Lines in STIS Spectra

λ_{lab} (Å, vac.)	Spectrum	log gf	E_{up} (cm^{-1})	γ Cru				α Ori			
				RV (km s^{-1})	FWHM (km s^{-1})	F_{int}	F_{surf}	RV (km s^{-1})	FWHM (km s^{-1})	F_{int}	F_{surf}
1196.670	Fe II	−1.09	104,817	−0.4	38	10.6	5.0	⋯	⋯	⋯	⋯
1199.236	Fe II	−0.02	104,817	−2.5	37	59.9	28.4	⋯	⋯	⋯	⋯
1199.671	Fe II	−0.11	104,938	8.5	35	37.9	18.0	⋯	⋯	⋯	⋯
1202.454	H2 1-2R3	−0.11	91,886	−1.7	39	10.8	5.1	⋯	⋯	⋯	⋯
1205.606	Fe II	−2.67	90,901	−10.0	60	32.0	15.1	⋯	⋯	⋯	⋯
1207.015	S I	⋯	82,849	−5.0	42	23.9	11.3	⋯	⋯	⋯	⋯
1207.760	S I	⋯	82,849	−1.0	26	6.9	3.3	⋯	⋯	⋯	⋯
1208.860	S I	⋯	82,723	−8.6	69	344.4	162.2	⋯	⋯	⋯	⋯
1209.431	Fe II	−1.79	90,639	−3.1	88	139.7	65.8	⋯	⋯	⋯	⋯
1209.829	Fe II	−4.37	91,048	10.3	61	46.8	22.0	⋯	⋯	⋯	⋯
1211.220	S I	⋯	82,562	−3.1	97	216.6	101.8	⋯	⋯	⋯	⋯
1212.820	S I	⋯	82,850	−10.3	64	37.8	17.8	⋯	⋯	⋯	⋯
1220.162	S I	⋯	82,352	−3.2	99	421.2	196.7	⋯	⋯	⋯	⋯
1220.872	Fe II	−2.01	90,301	−3.2	54	54.7	25.5	⋯	⋯	⋯	⋯
1221.492	Cr II	−0.60	94,363	1.7	50	92.1	43.0	⋯	⋯	⋯	⋯
1222.330	S I	⋯	82,208	−2.3	47	67.2	31.3	⋯	⋯	⋯	⋯
1224.990	S I	⋯	82,208	−4.1	43	30.3	14.1	⋯	⋯	⋯	⋯
1237.544	H2 2-2R11	0.35	95,229	0.8	31	3.9	1.8	⋯	⋯	⋯	⋯
1237.880	H2 1-2P8	−0.30	92,516	−4.0	31	14.8	6.8	⋯	⋯	⋯	⋯
1241.890	S I	⋯	80,521	9.2	38	4.8	2.2	⋯	⋯	⋯	⋯
1247.160	S I	−0.79	80,182	−2.5	32	7.7	3.5	⋯	⋯	⋯	⋯
1253.325	S I	−1.06	80,184	−2.0	28	6.1	2.8	⋯	⋯	⋯	⋯
1253.659	H2 4-4 R3	−0.45	95,584	−5.0	28	4.6	2.1	⋯	⋯	⋯	⋯
1254.129	H2 3-1 P17	−2.16	97,990	−0.7	28	8.6	3.9	⋯	⋯	⋯	⋯
1256.093	S I	−1.42	80,186	−3.0	18	2.1	1.0	⋯	⋯	⋯	⋯
1257.826	H2 1-3R3	−0.12	91,886	−1.2	28	52.3	23.8	−4.3	42	4.0	0.7
⋯	⋯	⋯	⋯	⋯	⋯	⋯	⋯	⋯	⋯	⋯	⋯

Note. Here F_{int} is the integrated line flux observed at Earth, while F_{surf} is the integrated line flux at the surface of the star; F_{int} is in units of 10^{-15} erg cm^{-2} s^{-1}, and F_{surf} is in units of erg cm^{-2} s^{-1}. Velocities are all relative to the stellar RV of 20.6 km s^{-1} for γ Cru and 21.9 for α Ori.

(This table is available in its entirety in machine-readable form.)

Table 8
Properties of Chromospheric and Wind Lines in the γ Cru ASTRAL Spectrum

λ (Å, vac.)	Spectrum	log gf	τ_{lte}	E_{low}	E_{high}	RV (km s^{-1})			FWHM (km s^{-1})			F_{int}	F_{surf}	W_{λ} (Å)	
						em	abs1	abs2	em	abs1	abs2	em	em	abs1	abs2
1244.535	C I	−3.80	−4.8	10,193	90,544	−4.1	⋯	⋯	26	⋯	⋯	4.4	2.0	⋯	⋯
1245.183	C I	−3.90	−4.9	10,193	90,502	−1.6	⋯	⋯	19	⋯	⋯	3.3	1.5	⋯	⋯
1245.964	C I	−3.45	−4.4	10,193	90,452	6.7	⋯	⋯	35	⋯	⋯	13.3	6.1	⋯	⋯
1246.176	C I	−3.73	−4.7	10,193	90,438	−0.6	⋯	⋯	17	⋯	⋯	1.7	0.8	⋯	⋯
1246.862	C I	−3.57	−4.5	10,193	90,394	0.2	⋯	⋯	30	⋯	⋯	5.5	2.5	⋯	⋯
1247.867	C I	−3.57	−4.5	10,193	90,329	−8.1	⋯	⋯	30	⋯	⋯	7.0	3.2	⋯	⋯
1248.009	C I	−3.67	−4.6	10,193	90,320	1.3	⋯	⋯	38	⋯	⋯	8.3	3.8	⋯	⋯
1248.993	C I	−3.67	−4.6	10,193	90,257	0.4	⋯	⋯	22	⋯	⋯	2.4	1.1	⋯	⋯
1249.405	C I	−3.38	−4.3	10,193	90,231	−1.9	⋯	⋯	23	⋯	⋯	4.2	1.9	⋯	⋯
1250.403	C I	−3.58	−4.5	10,193	90,167	2.7	⋯	⋯	17	⋯	⋯	2.5	1.1	⋯	⋯
1251.176	C I	−3.21	−4.2	10,193	90,117	−1.1	⋯	⋯	31	⋯	⋯	6.5	3.0	⋯	⋯
1252.208	C I	−3.28	−4.2	10,193	90,051	−5.0	⋯	⋯	28	⋯	⋯	4.5	2.1	⋯	⋯
1253.468	C I	−3.47	−4.4	10,193	89,971	−3.4	⋯	⋯	37	⋯	⋯	6.2	2.8	⋯	⋯
1254.525	C I	−3.16	−4.1	10,193	89,904	−3.3	⋯	⋯	23	⋯	⋯	3.3	1.5	⋯	⋯
1256.498	C I	−2.96	−3.9	10,193	89,779	4.9	⋯	⋯	37	⋯	⋯	7.3	3.3	⋯	⋯
1257.578	C I	−2.94	−3.9	10,193	89,710	−2.5	⋯	⋯	31	⋯	⋯	4.0	1.8	⋯	⋯
1258.798	Si I	−0.35	−0.3	223	79,663	−8.1	⋯	⋯	27	⋯	⋯	3.5	1.6	⋯	⋯
1261.737	C I	−2.95	−3.9	10,193	89,448	−6.7	⋯	⋯	33	⋯	⋯	5.4	2.4	⋯	⋯
1267.596	C I	−2.92	−3.9	10,193	89,082	0.6	⋯	⋯	22	⋯	⋯	4.8	2.2	⋯	⋯
1274.756	C I	−3.33	−4.3	10,193	88,639	−2.0	⋯	⋯	23	⋯	⋯	9.6	4.3	⋯	⋯
1276.287	C I	−2.73	−3.7	10,193	88,545	−1.2	⋯	⋯	29	⋯	⋯	9.0	4.0	⋯	⋯
1288.037	C I	−3.67	−4.6	10,193	87,830	−5.1	⋯	⋯	26	⋯	⋯	5.4	2.4	⋯	⋯
1288.422	C I	−1.54	−2.5	10,193	87,807	−1.0	⋯	⋯	31	⋯	⋯	12.2	5.4	⋯	⋯
1289.984	C I	−2.44	−3.4	10,193	87,713	−4.4	⋯	⋯	28	⋯	⋯	8.4	3.7	⋯	⋯
1291.304	C I	−2.32	−3.3	10,193	87,634	1.2	⋯	⋯	23	⋯	⋯	4.4	2.0	⋯	⋯
1302.168	O I	−0.59	−0.5	0	76,795	−2.2	−4.2	−31.2	64	54	17	8320.3	3681.7	150.4	3.4
1304.858	O I	−0.81	−0.7	158	76,794	−0.1	5.2	−16.1	50	31	27	7447.4	3290.7	10.9	6.1
1306.029	O I	−1.29	−1.2	227	76,794	−2.4	8.5	−11.9	54	24	33	5984.1	2642.5	35.3	86.0
⋯	⋯	⋯	⋯	⋯	⋯	⋯	⋯	⋯	⋯	⋯	⋯	⋯	⋯	⋯	

Note. Here F_{int} is in units of 10^{-15} erg cm^{-2} s^{-1}, and F_{surf} is in units of erg cm^{-2} s^{-1}.

(This table is available in its entirety in machine-readable form.)

Table 9
Properties of Chromospheric and Wind Lines in the α Ori ASTRAL Spectrum

λ (Å, vac.)	Spectrum	log gf	τ_{lte}	E_{low}	E_{high}	RV (km s^{-1})			FWHM (km s^{-1})			F_{int}	F_{surf}	W_{λ} (Å)	
						em	abs1	abs2	em	abs1	abs2	em	em	abs1	abs2
1245.964	C I	−3.45	−4.4	10,193	90,452	−3.6	⋯	⋯	15	⋯	⋯	0.3	0.1	⋯	⋯
1246.176	C I	−3.73	−4.7	10,193	90,438	−31.8	⋯	⋯	59	⋯	⋯	2.2	0.4	⋯	⋯
1302.168	O I	−0.59	−0.5	0	76,795	⋯	⋯	⋯	⋯	⋯	⋯	⋯	⋯	⋯	⋯
1302.862	S I	−1.07	−1.0	396	77,150	−1.7	−3.7	12.4	41	29	18	109.0	19.2	30.1	4.6
1304.858	O I	−0.84	−0.7	158	76,794	10.9	0.7	25.4	65	48	32	157.8	27.8	10.9	3.2
1306.029	O I	−1.32	−1.2	227	76,794	−3.4	−24.4	7.6	72	44	44	253.5	44.5	8.4	10.5
⋯	⋯	⋯	⋯	⋯	⋯	⋯	⋯	⋯	⋯	⋯	⋯	⋯	⋯	⋯	

Note. Here F_{int} is in units of 10^{-15} erg cm^{-2} s^{-1}, and F_{surf} is in units of erg cm^{-2} s^{-1}.

(This table is available in its entirety in machine-readable form.)

ORCID iDs

Kenneth G. Carpenter https://orcid.org/0000-0002-0706-079X
Thomas R. Ayres https://orcid.org/0000-0002-1242-5124
Gioia Rau https://orcid.org/0000-0002-3042-4539

References

Ayres, T. R. 1986, ApJ, 308, 246
Ayres, T. R., Brown, A., Harper, G. M., et al. 1999, BAAS, 31, 930
Ayres, T. R., Judge, P., Jordan, C., Brown, A., & Linsky, J. L. 1986, ApJ, 311, 947
Ayres, T. R., Moos, H. W., & Linsky, J. L. 1981, ApJL, 248, L137
Bernat, A. P., Honeycutt, R. K., Kephart, J. E., et al. 1978, ApJ, 219, 532
Blackwell, D. E., & Shallis, M. J. 1977, MNRAS, 180, 177
Boesgaard, A. M. 1979, ApJ, 232, 485
Boesgaard, A. M., & Magnan, C. 1975, ApJ, 198, 369
Bohn, H. U. 1984, A&A, 136, 338
Brandt, J. C., Heap, S. R., Beaver, E. A., et al. 1995, AJ, 109, 2706
Carpenter, K. G. 1984, ApJ, 285, 181
Carpenter, K. G., Ayres, T. R., Harper, G. M., et al. 2014, ApJ, 794, 41
Carpenter, K. G., & Johansson, S. 1988, in ESA Spec. Pub., A Decade of UV Astronomy with the IUE Satellite, ed. E. Rolfe (Noordwijk: ESA), 349
Carpenter, K. G., Pesce, J. E., Stencel, R. E., et al. 1988, ApJS, 68, 345

Carpenter, K. G., & Robinson, R. D. 1997, ApJ, 479, 970
Carpenter, K. G., Robinson, R. D., Harper, G. M., et al. 1999, ApJ, 521, 382
Carpenter, K. G., Robinson, R. D., & Judge, P. G. 1995, ApJ, 444, 424
Carpenter, K. G., Robinson, R. D., Wahlgren, G. M., Linsky, J. L., & Brown, A. 1994, ApJ, 428, 329
Glindemann, A., Bauvir, B., Delplancke, F., et al. 2001, Astronomische Gesellschaft Abstract Ser. 18, #MS 06 06
Goldberg, L. 1984, PASP, 96, 366
Harper, G. M., Brown, A., & Guinan, E. F. 2008, AJ, 135, 1430
Haubois, X., Perrin, G., Lacour, S., et al. 2009, A&A, 508, 923
Hempe, K., & Reimers, D. 1982, A&A, 107, 36
Hinkle, K., Wallace, L., Valenti, J., & Ayres, T. 2005, Ultraviolet Atlas of the Arcturus Spectrum, 1150–3800 A (San Francisco, CA: ASP)
Johansson, S., Brage, T., Leckrone, D. S., Nave, G., & Wahlgren, G. M. 1995, ApJ, 446, 361
Johansson, S., & Jordan, C. 1984, MNRAS, 210, 239
Jordan, C. 1967, SoPh, 2, 441
Judge, P. G. 1986, MNRAS, 221, 119

Judge, P. G. 1988, MNRAS, 231, 419
Judge, P. G., & Stencel, R. E. 1991, ApJ, 371, 357
Kiehling, R. 1987, A&AS, 69, 465
Lobel, A., & Dupree, A. K. 2000, ApJ, 545, 454
Lobel, A., & Dupree, A. K. 2001, ApJ, 558, 815
McDonald, I., Zijlstra, A. A., & Watson, R. A. 2017, MNRAS, 471, 770
McMurry, A. D., & Jordan, C. 2000, MNRAS, 313, 423
Ohnaka, K., Weigelt, G., Millour, F., et al. 2011, A&A, 529, A163
Pérez Martínez, M. I., Schröder, K.-P., & Cuntz, M. 2011, MNRAS, 414, 418
Perrin, G., Ridgway, S. T., Coudé du Foresto, V., et al. 2004, A&A, 418, 675
Petit, V., Owocki, S. P., Wade, G. A., et al. 2013, MNRAS, 429, 398
Ramírez, I., & Allende Prieto, C. 2011, ApJ, 743, 135
Rau, G., Nielsen, K. E., Carpenter, K. G., & Airapetian, V. 2018, ApJ, 869, 1
Shine, R. A. 1983, ApJ, 266, 882
Tessore, B., Lèbre, A., Morin, J., et al. 2017, A&A, 603, A129
Tondello, G. 1972, ApJ, 172, 771
Weymann, R. 1962, ApJ, 136, 844
Wood, B. E., Müller, H.-R., & Harper, G. M. 2016, ApJ, 829, 74